



This is an electronic reprint of the original article. This reprint may differ from the original in pagination and typographic detail.

Semkin, Vasilii; Haarla, Jaakko; Pairon, Thomas; Slezak, Christopher; Rangan, Sundeep; Viikari, Ville; Oestges, Claude

## Analyzing Radar Cross Section Signatures of Diverse Drone Models at mmWave Frequencies

Published in: **IEEE Access** 

10.1109/ACCESS.2020.2979339

Published: 01/01/2020

Document Version Publisher's PDF, also known as Version of record

Published under the following license: CC BY

Please cite the original version: Semkin, V., Haarla, J., Pairon, T., Slezak, C., Rangan, S., Viikari, V., & Oestges, C. (2020). Analyzing Radar Cross Section Signatures of Diverse Drone Models at mmWave Frequencies. IEEE Access, 8, 48958-48969. Article 9032332. https://doi.org/10.1109/ACCESS.2020.2979339

This material is protected by copyright and other intellectual property rights, and duplication or sale of all or part of any of the repository collections is not permitted, except that material may be duplicated by you for your research use or educational purposes in electronic or print form. You must obtain permission for any other use. Electronic or print copies may not be offered, whether for sale or otherwise to anyone who is not an authorised user.



Received February 5, 2020, accepted February 19, 2020, date of publication March 11, 2020, date of current version March 19, 2020.

Digital Object Identifier 10.1109/ACCESS.2020.2979339

# **Analyzing Radar Cross Section Signatures of Diverse Drone Models at mmWave Frequencies**

VASILII SEMKIN<sup>®</sup>1,2, JAAKKO HAARLA<sup>®</sup>3, THOMAS PAIRON<sup>®</sup>1, CHRISTOPHER SLEZAK<sup>®</sup><sup>4</sup>, (Student Member, IEEE), SUNDEEP RANGAN<sup>®</sup><sup>4</sup>, (Fellow, IEEE), VILLE VIIKARI<sup>®3</sup>, (Senior Member, IEEE), AND CLAUDE OESTGES<sup>®1</sup>, (Fellow, IEEE)

¹ICTEAM, Université catholique de Louvain, 1348 Louvain-la-Neuve, Belgium

²VTT Technical Research Centre of Finland Ltd., 02150 Espoo, Finland

Corresponding author: Vasilii Semkin (vasilii.semkin@vtt.fi)

This work was supported in part by the MACHAON Project funded by the Belgian Science Foundation FRS-FNRS (Fonds de la Recherche Scientifique), in part by the MUSEWINET Project through the Belgian Science Foundation EOS Program, and in part by the Framework of COST Action CA15104 IRACON. The work of Christopher Slezak and Sundeep Rangan was supported in part by NSF under Grant 1302336, Grant 1564142, Grant 1547332, and Grant 1824434, in part by NIST, in part by SRC, and in part by the industrial affiliates of NYU WIRELESS.

**ABSTRACT** In this work, we present quasi-monostatic Radar Cross Section measurements of different Unmanned Aerial Vehicles at 26-40 GHz. We study the Radar Cross Section signatures of nine different multi-rotor platforms as well as a single Lithium-ion Polymer battery. These results are useful in the design and testing of radar systems which employ millimeter-wave frequencies for superior drone detection. The data shows how radio waves are scattered by drones of various sizes and what impact the primary construction material has on the received Radar Cross Section signatures. Matching our intuition, the measurements confirm that larger drones made of carbon fiber are easier to detect, whereas drones made from plastic and styrofoam materials are less visible to the radar systems. The measurement results are published as an open database, creating an invaluable reference for engineers working on drone detection.

**INDEX TERMS** Drone detection, millimeter-wave, radar cross section, unmanned aerial vehicle.

#### I. INTRODUCTION

Recently, unmanned aerial vehicles (UAVs) have captured the interest of the academy, industry and general public due to their enormous potential. These UAVs (also often referred to as drones) are useful in a wide range of applications such as: cinematography, agriculture, mapping, forensics, stockpile measurements, shipping, law enforcement, mobile communication and many others. As wireless communication technologies evolve to enable higher data rates and lower latency, new application areas are emerging, e.g., drone assisted driving. As exciting as these new applications are, it is important to recognize that the misuse of drone technology presents a real threat for privacy, property damage, and the health and safety of the public. The anticipated explosion in the number of UAVs [1] will require more stringent regulations and control by the authorities. However, these new regulations can be violated unintentionally or even deliberately. In comparison to other more established technologies such as cars, drones

The associate editor coordinating the review of this manuscript and approving it for publication was Vittorio Degli-Esposti

present a unique challenge when it comes to the enforcement of regulations that govern how a drone may behave.

In the last few years, there have been numerous episodes when drone operators violated regulations and have used drones in the restricted areas. Such incidents can lead to catastrophic economic consequences and, more importantly, can present a real danger to people's lives. Nowadays, the drone regulation topic is under development and, possibly, common rules will be applied for all countries in the EU in the near future.<sup>2</sup> However, there might be custom built unregistered drones flying in the restricted areas. Undoubtedly, it is more difficult to detect drones due to their small dimensions relative to other moving objects, for example cars. Typical maximum radar cross section (RCS) values for consumer cars vary around average values of 18 dBsm at 23-27 GHz and 25 dBsm at 76-81 GHz [2], [3]. On the other hand, typical RCS value for drones are from -15 to -20 dBsm in the X-band [4] and smaller than -20 dBsm at 30-37 GHz [5].

<sup>&</sup>lt;sup>3</sup> Aalto University School of Electrical Engineering, 02150 Espoo, Finland

<sup>&</sup>lt;sup>4</sup>NYU WIRELESS, NYU Tandon School of Engineering, Brooklyn, NY 11201, USA

<sup>&</sup>lt;sup>1</sup>https://en.wikipedia.org/wiki/List\_of\_UAV-related\_incidents

<sup>&</sup>lt;sup>2</sup>https://www.easa.europa.eu



This shows the urgent need for better technologies to monitor the presence of drones and prevent possible threats.

One possible method to detect malignant drones is to employ millimeter-wave (mmWave) radar systems. With the release of the new 5G New Radio (NR) standard, cellular networks are shifting to higher frequency bands such as 28 GHz due to the large available bandwidth and less probable interference [6]. The use of mmWave frequencies in the radar systems has some advantages, e.g. better resolution, and makes it possible to detect smaller objects. Based on the measured RCS signatures the flying object can be identified and necessary actions can be undertaken by the authorities. Cellular operators have already begun deploying the new infrastructure required for 5G NR, and soon 5G base stations operating at mmWave frequencies will be densely deployed in cities. Adopting this infrastructure for drone detection would result in a great cost savings, since the work of provisioning and deploying the equipment would already be handled by cellular operators. Recent work has shown that these base stations could operate as a radar with small modifications [7].

In this work, we provide extensive measurement results of diverse drone models at one possible 5G frequency band along with a study of the particular drone's frame materials. In addition, we estimate the effect of different drone parts on the total RCS values through simulation results. A large number of the research papers (e.g. [5], [8]–[12]), in which authors study the RCS signatures of drones at different frequencies, show the relevance and impact of this topic. For example, in [8], the authors present measurement results of the DJI Phantom drone using a 94 GHz radar system. In [9], the RCS of two consumer drone models are presented in the 5.8 to 8.2 GHz frequency range. Another research work [5], provides wideband RCS measurements of non-metallic objects at 30-37 GHz. RCS results obtained using a K<sub>u</sub> band radar are presented in [10]. However, in the previous research activities only a handful of drone models (with a limited range of materials) were studied and many frequencies were not covered. In addition, there is a lack of RCS covering full or quasi-3D space. Following a similar framework to the measurements above, we aim to fill the gap and present comprehensive 3D measurements of RCS characteristics of nine UAVs as well as the RCS of the Li-Po batteries, since the batteries are the immense reflective object in the drone configuration. In this work, we study quasi-3D RCS signatures of a diverse range of drone models over the frequency band of 26-40 GHz, which may provide essential material for the drone database.<sup>3</sup> With this database, researchers who lack the expertise, equipment or facilities to perform these RCS measurements themselves can develop new techniques to detect drones. For example, Machine Learning researchers can use this data to test the effectiveness of the many tools available in their field of research to see if they can advance the state-of-the-art in drone detection.

The structure of this document is as follows: Section II presents the basic principle of radio detection, a description of the measurement setup, and overview of the studied drone models. Section III provides the analysis of the calibration measurement results, measured RCS signatures of drones<sup>3</sup>, and preliminary simulation results estimating the effect of different drone parts on the RCS characteristics. Finally, Section IV concludes the paper, discusses the obtained results, and describes the plan for the future work. The appendix includes measured RCS values along with mean and standard deviation for the frequency range from 26 GHz to 40 GHz.

#### **II. METHODOLOGY**

In this work, we perform quasi-monostatic RCS measurements of different types of drones. The frequency range of 26 to 40 GHz is covered in 1 GHz increments.

#### A. RADIO DETECTION PRINCIPLE

There are several methods of radio detection and ranging available: monostatic, quasi-monostatic and bistatic. For the monostatic case the transmitter (Tx) and receiver (Rx) are spatially co-located, i.e. in practice the same antenna is used both for transmission and reception. In the bistatic configuration the transmit and receive antennas are placed at different locations. The quasi-monostatic case refers to the setup where different antennas are used for Tx and Rx but they are placed as close to each other as their physical dimensions allow. In this work, we utilize the quasi-monostatic approach to characterize the different targets. By transmitting a signal from the Tx antenna and monitoring for reflections that arrive at the Rx antenna, we can determine if the target is present, identify moving parts of the target (such as propellers), and make an estimation of possible drone models. For the quasi-monostatic case the received power is determined by the radar equation [13]:

$$P_r = \frac{P_t G_t G_r \sigma \lambda^2}{(4\pi)^3 R^4}.$$
 (1)

In Eq. (1)  $P_t$  is the transmitted power,  $G_t$  is the transmitter antenna gain,  $G_r$  is the receiver antenna gain,  $\lambda$  is the wavelength,  $\sigma$  is the quasi-monostatic radar cross section in  $m^2$ , and R is the distance to the target. It should be noted, that the RCS is generally a function of the direction of the transmitter antenna and the receiver antenna with respect to the target. In this quasi-monostatic case we assume both angles to be approximately the same. The antenna parameters, distance to the target, and the transmitted power are known, while the received power is obtained via measurements. Hence, the radar cross section is the only unknown quantity in this equation and can easily be calculated.

## **B. MEASUREMENT EQUIPMENT**

To ensure that the only reflections present were from the target, measurements were performed in an anechoic chamber at Aalto University, Finland. The anechoic chamber, which was

 $<sup>^3</sup> The$  measurement data is available as a supplementary material. http://dx.doi.org/10.21227/m8xk-dr55



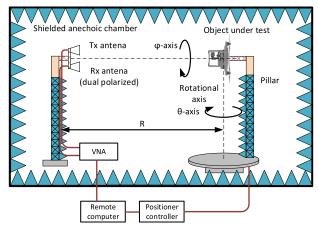


FIGURE 1. The schematic view of the measurement setup.

originally constructed for antenna pattern measurements, was modified to better serve RCS measurements. The schematic view of the measurement setup is presented in Fig. 1. The Tx and Rx antennas are mounted on the mast at one end of the anechoic chamber, consistent with the definition of quasi-monostatic radar. A standard gain horn antenna is used at the Tx side, while a dual polarized Vivaldi horn antenna is used as the Rx. A VNA is used as a generator and also to record the received signal. The measurements were performed at 26-40 GHz (1 GHz step) with an IF bandwidth of 1 kHz. It takes approximately 5 hours to measure one drone model, therefore, two sets of measurements were performed at different periods. One set with an amplifier in the Tx path and one without the amplifier (due to unavailability during the second set of measurements). The transmitted power was set to -20 dBm and an amplifier was used in the Tx signal path to achieve the desired input power to the antenna, while for the second set, without power amplifier, 0 dBm input power was used. Before conducting each set of measurements, a back-to-back calibration was performed. During this measurement, the RF output port of the Tx is connected to the RF input port of the Rx through a 20 dB attenuator. By performing such calibration, any losses in the cables and the equipment can be taken into account and the reference signal level is obtained. The object under test (OUT) is located on top of a rotating pillar on the opposite side of the chamber than antennas. Stepped motors allow two axes of rotation of the OUT. First, the object is rotated in the azimuth plane  $(\theta$ -axis), then it is rolled around the center axis  $(\phi$ -axis). Angular ranges were set to  $\theta \in [-90^{\circ}, 90^{\circ}]$  and  $\phi \in$ [0°, 180°] with steps of 1°. For each UAV, the bottom hemisphere was measured. In this way, we replicate the realistic scenario when the UAV is illuminated by a radar station located on the ground. In addition, measuring only half of the sphere significantly reduces the measurement time. The distance R between the test antennas and the OUT is 5.8 m.

## C. INVESTIGATED DRONE MODELS

In this measurement campaign, eight multi-rotor platforms, one radio-controlled (RC) helicopter, and one 6-cell Li-Po battery were measured. Photographs of the studied drones

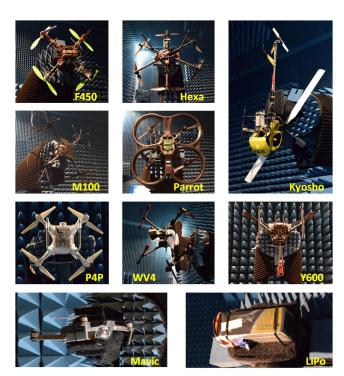


FIGURE 2. Photographs of the empirically studied objects (i.e. multirotor platforms, helicopter, battery).

are presented in Fig. 2, while all the dimensions as well as the materials of the measured objects are summarized in Table 1. The most popular drones with different configurations (e.g. quadrocopters with X-shape, H-shape frame, hexacopter, Y-shape tricopter, etc.) were selected for the RCS measurements in order to provide a representative sample of available UAVs. The largest drone models are a custom built hexacopter, DJI Matrice M100 quadrocopter, HMF Y600, and Walkera Voyager 4. On the DJI Matrice M100 protective cages were mounted during the measurements, increasing the drone size. However, these cages do not have a significant effect on the RCS since they are made from plastic material (this is demonstrated in the analysis shown in Section III.) These drones all have carbon fiber frames. In addition, carbon fiber propellers are installed on the DJI Matrice M100 and custom built hexacopter, while the other drone models have plastic propellers. There were no installed electronics or any other components installed on the HMF Y600 (only the frame was measured). The other investigated drones are mainly made of plastic material (DJI Mavic Pro, DJI Phantom 4 Pro, helicopter Kyosho, and DJI F450) and styrofoam (Parrot AR.Drone). The helicopter frame is plastic with a plastic propeller. It should be noted that the diagonal dimensions for the multi-rotor platforms exclude propellers, except the Parrot drone. The Parrot drone dimensions include also the outer frame since the propellers are located inside the frame. Each drone was measured with an attached battery, corresponding to the drone dimensions. The exceptions are the HMF Y600 and custom built hexacopter. Only the frame of the tri-copter HMF Y600 was measured. On the hexacopter two aluminium blocks were used to replicate the batteries



TABLE 1. The measured drone types and their parameters.

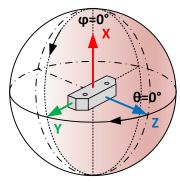
Measured object	Dimensions (mm)	Main material	VV (set Nº)		НН	HH (set Nº)		I/HV ∶Nº)	Group	
DJI Mavic Pro	Diagonal, 335	Plastic			✓	(1)			I	
DJI F450	Diagonal, 450	Plastic			$\checkmark$	(1)			I	
DJI Matrice 100	Diagonal, 650	Carbon fiber	$\checkmark$	(2)	$\checkmark$	(1,2)	$\checkmark$	(2)	II	
Parrot AR.Drone	Diagonal, 580	Styrofoam			$\checkmark$	(1)			I	
Custom built Hexacopter	Diagonal, 900	Carbon fiber	$\checkmark$	(2)	$\checkmark$	(1)			II	
Helicopter Kyosho	$780\times130\times200$	Plastic			$\checkmark$	(1)			I	
DJI Phantom 4 Pro	Diagonal, 350	Plastic	$\checkmark$	(2)	$\checkmark$	(2)			I	
HMF Y600	Diagonal, 600	Carbon fiber	$\checkmark$	(2)	$\checkmark$	(2)			II	
Walkera Voyager 4	$465\times465\times352$	Carbon fiber	$\checkmark$	(2)	$\checkmark$	(2)			II	
Battery 6S LiPo	$170\times50\times50$	Lithium-ion polymer			$\checkmark$	(1)			I	

in order to decrease the drone weight and avoid overloading the rotational pillar in the anechoic chamber. Since the Li-Po battery is one of the largest reflective object in any drone model, similar measurements of the RCS of the Li-Po battery were performed separately. The largest battery available was used in these measurements, a Li-Po 6-cell battery with a capacity of 10000 mAh. For example, two of these batteries are used to operate the custom built hexacopter during normal use.

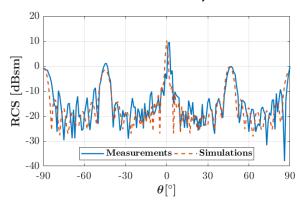
#### **III. MEASUREMENT AND SIMULATION RESULTS**

#### A. CALIBRATION MEASUREMENTS

First, we verify that the presented measurement setup can be utilized for the RCS measurements and meaningful results can be obtained. In order to do that, we perform RCS measurements and simulations of a reference target. The reference trapezoidal cuboid and the employed coordinate system are presented in Fig. 3a. The longest dimension of the cuboid is 180 mm, and the front side is 128 mm long. The width is 60 mm (along the Z-axis). The height is 53 mm (dimension along X-axis). The cuboid is made from aluminum. To demonstrate the validity of the measurement setup, the RCS of an identical cuboid was calculated via electromagnetic simulations in the CST Microwave Studio ray tracing tool. Ray tracing simulations are faster than Integral Equation solver and may achieve the same accuracy for basic-shaped objects such as parallelepipeds. Fig. 3b shows the measured and simulated RCS characteristic of the cuboid at 40 GHz in the YZ-plane, i.e.  $\phi = 90^{\circ}$ , and  $\theta = \pm 90^{\circ}$ . Besides a small misalignment, there is a fair comparison between the measurement and the simulation results. The strong reflections can be observed at  $\theta = \pm 90^{\circ}$ ,  $\theta = \pm 45^{\circ}$ , and  $\theta = 0^{\circ}$ , as expected for an object of this shape. A maximum value of 10.2 dBsm is obtained. Differences are visible away from the specular reflections due to the asymptotic solver used in the simulations. At several points there are small peaks visible in the measured results that are not seen in the simulated results. This was empirically verified and was found to be caused by the rotational pillar of the measurement system. In general, we note that there is a good agreement between the measurement and the simulation.



(a) Schematic view of the reference object: trapezoidal cuboid and the relevant coordinate system.



(b) Simulated and measured RCS of the cuboid at 40 GHz in the YZ-plane. Simulations are performed with ray-tracing in CST Microwave Studio.

FIGURE 3. The schematic view of the cuboid and the relevant coordinate system.

#### B. ANALYZING THE RCS SIGNATURES

In this section, the analysis of the measured RCS signatures of different drone models (see Fig. 2) is presented. It is likely that radar systems will observe drones from below. Under this assumption, only the bottom hemisphere of the drones was measured (highlighted region in Fig. 3a). Based on the obtained measurement results all studied objects were divided into two groups. The first group contains the Li-Po battery and small drones made of plastic (DJI F450, DJI Phantom 4 Pro, DJI Mavic, Parrot, helicopter Kyosho), while

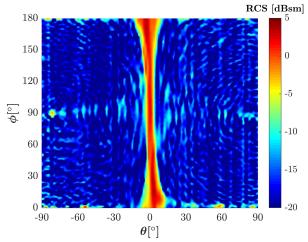


FIGURE 4. RCS signature of the 6S Li-Po battery at 28 GHz.

the second group includes large drone models made of carbon fiber material (DJI Matrice M100, custom build hexacopter, Walkera Voyager 4, and HMF Y600). It is necessary to mention, that obtained results are presented for the near field (NF) or semi-far-field, depending on the frequency and the measured model. According to our assumption, the total scattered power measured in semi-far-field and far-field are approximately the same, whereas the RCS patterns may have slightly different shapes in the angular domain. In practice, however, the differences are likely very small (especially because none of the drones have long, perfectly flat surfaces or long straight edges, except Li-Po batteries, that would conserve plane waves after reflection). In addition, the measurements were performed only for one Tx polarization and only for bottom hemisphere, which complicates the NF to FF transformation and is not in a scope of this paper. However, the measured data is available as a supplementary material<sup>3</sup> and NF to FF transformation may be applied later [14]-[16]. The presented results give an insight on drone detection and still might be useful for developing detection methods and systems.

#### 1) SMALL DRONES MADE OF PLASTIC MATERIALS

For any drone, batteries play a substantial role in the total reflected power [17], [18]. Even if the drone is fully made of plastic or styrofoam the battery will be a large "metallic" object which reflects a substantial amount of energy. Therefore, we present the RCS of the battery first. As will be shown later, the RCS of the standalone measured battery is similar to the RCS measured from small plastic drones.

In Fig. 4, the RCS signature of the 6-cell Li-Po battery is presented. The strongest reflections are obtained when the battery is illuminated from  $\theta=0^{\circ}$  for all  $\phi$  angles. The strongest reflection is observed when the larger face of the battery is illuminated. In addition, one can see some reflections for all  $\theta$  angles at  $\phi=0,90,180^{\circ}$ . Generally, the geometry of the battery is similar to that one of a rectangular cuboid, therefore, the RCS characteristic will also match.

In Fig. 5, the RCS signatures at 28 and 38 GHz of the drones from the first group, i.e. quadrocopters DJI F450, Phantom 4 Pro, DJI Mavic Pro, and helicopter, are presented.

One can observe that the RCS of the DJI F450 is very similar to the RCS of the Li-Po battery shown in Fig. 4. The strongest RCS values are obtained for  $\theta=0^\circ$  and for all  $\phi$  angles, as well as, for  $\phi=90^\circ$  and all  $\theta$ . The arms of the quadrocopter DJI F450 are made of plastic with a honeycomb structure. In the center of the drone, there is a board with the electronics and, usually, on the bottom, the battery is located. The battery is the largest reflective object in this drone model and this is exactly what can be seen from the RCS signatures (Fig. 5a and 5b).

The next drone model to be analyzed is DJI Phantom 4 Pro. This model is the most popular among amateurs and professionals for its low price and large capabilities in different applications. The received power levels (Fig. 5d and 5e, P4P) are a bit different from the received RCS signature of DJI F450. However, the battery structure is also visible on the RCS plot. The main difference between the RCS characteristic of the DJI Phantom and the DJI F450 is that the Phantom does not have high reflections received at  $\phi = 90^{\circ}$  for all  $\theta$ angles. There are a lot of reflections all over  $\theta$  and  $\phi$  angles observed in Fig. 5d and 5h. There are more electronics and a larger amount of wires in this drone model when compared to the quadrocopter DJI F450. Therefore, we assume that all the electronics, GPS antennas and dense wires inside the Phantom 4 drone increase the baseline of the RCS characteristic by scattering the signal to many different directions. The DJI Mavic Pro (Fig. 5g and Fig. 5h) has similar RCS characteristic to the Phantom. Hovewer, the maximum RCS values are lower than for the Phantom and DJI F450. This is due to the smaller size of this drone.

Last in this group is the RC helicopter (Fig. 5j and Fig. 5k). If we take a closer look at the RCS characteristic, we can verify that the RCS of the helicopter is also similar to the battery RCS. The difference is only that the orientation of the battery in helicopter was rotated 90° from that of the measured standalone battery. This means that the reflections which were visible for the battery at  $\phi=90$  and all  $\theta=0$  angles are relocated and are visible at angles  $\phi=0^\circ$  and  $\phi=180^\circ$ .

In this subsection, we have presented the measurement results of the RCS signatures of drones from the Group I. It was confirmed by the measurements that the drone battery has the largest impact on the small drone RCS.

In addition to the RCS characteristic, the probability density functions for these drone models are presented in Fig. 11. The PDF plot shows the distribution of average RCS values for each drone at 28 GHz. More detailed analysis is presented in the end of this section.

#### 2) LARGE AND CARBON FIBER DRONE MODELS

In this subsection, the RCS analysis for "large" drones made of carbon fiber material is provided (group II in Table 1). Carbon fiber material is very reflective due to its structure [19]. Hence, drones made from this material will be more visible to radar than the drones from the previous group. The RCS signatures for quadrocopter DJI Matrice M100, custom built



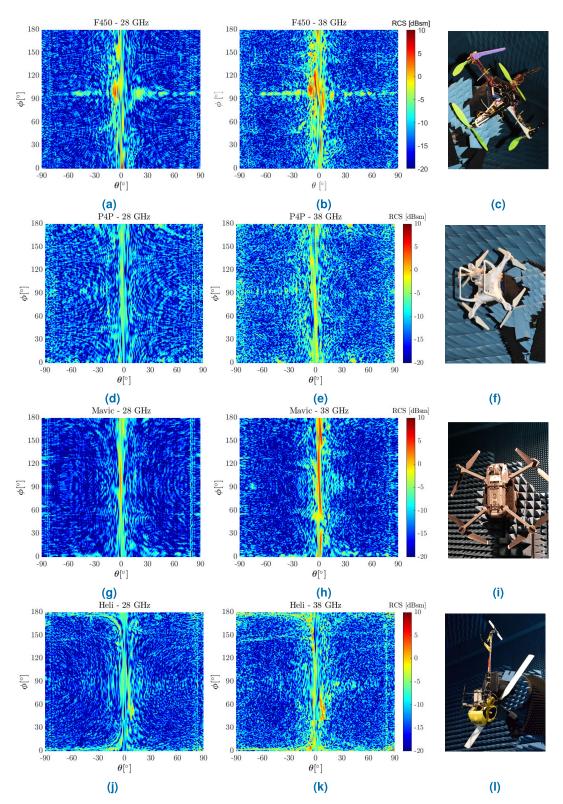


FIGURE 5. Monostatic RCS of drones from the Group I, with respect to the azimuth and elevation angles. Left(right) column corresponds to measurements at 28(38) GHz.

hexacopter, tricopter HMF Y600, and H-shape Walkera Voyager 4 are presented in Fig. 6. It must be noted that for the Y-shape tricopter HMF Y600 only the frame was measured. Specifically for this model all electronics were excluded from

the measurements to verify the idea that electronics and wires in the drone provide more reflections to all angles.

From Fig. 6, we can clearly identify the shape of each drone. For example, the carbon fiber arms of the hexacopter

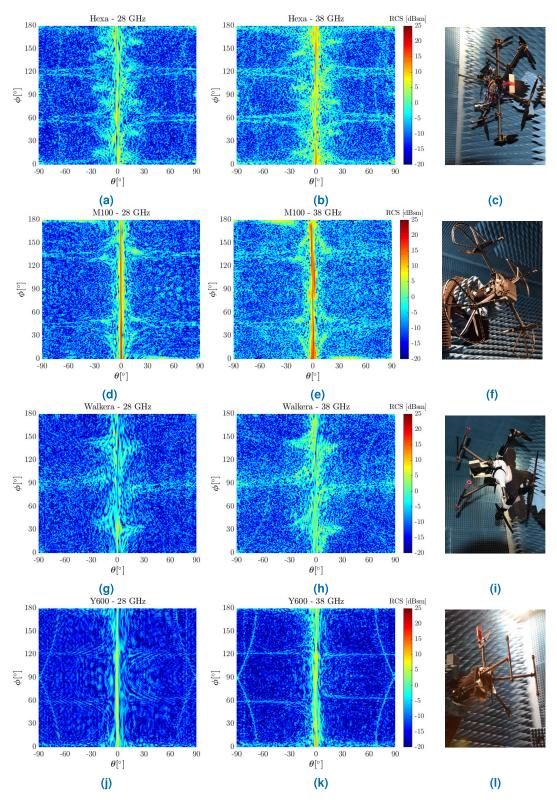


FIGURE 6. Monostatic RCS of drones from Group II, with respect to the azimuth and elevation angles. Left(right) column corresponds to measurements at 28(38) GHz.

can be seen at  $\phi=0^\circ$ ,  $60^\circ$ ,  $120^\circ$ , and  $180^\circ$ . Theoretically, the RCS signature should be symmetric for the measured hexacopter drone model. However, analyzing the RCS at 28 GHz for this drone, higher values of the RCS are obtained

between  $\phi=30^\circ$  and  $\phi=90^\circ$  (Fig. 6a), with  $\theta=0^\circ$ . This is owed by the drone misalignment in this particular measurement. By contrast, the next drone, which is DJI M100, is almost perfectly aligned and is perpendicular to the incident



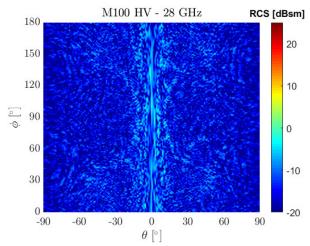


FIGURE 7. Cross-polarization RCS measurement of DJI M100 at 28 GHz.

wave. As a result, the RCS characteristic is fully symmetric (Fig. 6d) for all  $\phi$  angles, for fixed  $\theta=0^\circ$ . Additionally, a cross-polarization RCS measurement at 28 GHz for the DJI M100 is presented in Fig. 7. During this measurement the Tx was horizontally polarized, while the Rx was vertically polarized. These results provide additional insight on the drone RCS characteristic. As can be observed, the reflections for the cross-polarization measurement are weaker than in the corresponding co-polarization measurement (Fig. 6d and Fig. 7). Only the frame of the drone is visible, letting us conclude that combining the cross-polarized component with the co-polarization measurement will slightly increase received power levels only for the frame of the drone.

Another measured drone model in this group is the H-shaped Walkera Voyager 4. The RCS signatures are presented in Fig. 6g and Fig. 6h at 28 and 38 GHz, respectively. This drone was measured with a camera mounted on a gimbal as a payload. Since the shape of the hull of this drone is not flat, there were some difficulties in aligning this drone for the measurements. This resulted in small asymmetries which can be seen in the RCS signature. The RCS signatures of the Y-shaped HMF Y600 drone are provided in Figs. 6j and 6k. Only the frame of this drone was fixed on the rotational pillar. The reason behind was to test a drone without any electrical components, antennas and motors. As can be seen, the signatures of this tri-copter are more visible.

It is worth noting one distinctive feature for the hexacopter, Walkera Voyager 4, and HMF Y600, which is carbon fiber landing gear (Fig. 6c, 6i, 6l). These are used to protect the drone's payload and for safe take off and landing. The presence of this landing gear is apparent in the obtained RCS signatures (Fig. 6). Let us focus on the RCS values obtained at 38 GHz for these drone models. The hexacopter has three carbon fiber tubes acting as a chassis, which are slightly rotated relative to the perpendicular plane to the ground. The chassis is visible in Fig. 6b: two curved lines between  $\theta = -90^{\circ}$  and  $\theta = -60^{\circ}$  as well as one curved line between  $\theta = 60^{\circ}$  and  $\theta = 90^{\circ}$ . The Walkera Voyager has two carbon fiber landing gears, represented by two curved lines in the RCS figure.

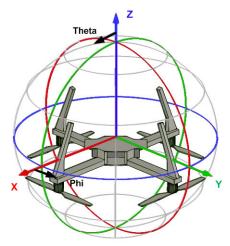


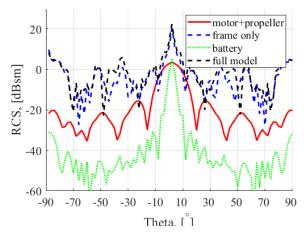
FIGURE 8. Drone model used in the simulations with relevant coordinate system.

The tricopter Y600 has similar landing gear to Walkera, however, the initial position of both drones was offset by 90°. Thus, there are two curves observed between the same  $\theta$  angles.

## 3) SIMULATION RESULTS OF DIFFERENT DRONE PARTS

In this subsection, we present simulation results obtained with the Integral Equation (IE) solver in CST Microwave Studio. We analyse the impact of different drone parts on the total RCS signature at 28 GHz. This provides a better understanding of what components affect the total drone RCS characteristics. The IE solver provides exact solution (comparing with ray tracing), however, simulation of bottom hemisphere at mmWave frequencies would be time consuming, therefore, only cuts at the specific angles are studied. The cuts for the following angles  $\phi = 0^{\circ} : 2^{\circ} : 180^{\circ}, \theta = 0^{\circ},$ and  $\theta = 45^{\circ}$  are presented in Fig. 8. A general drone model is used in the simulations. The drone material is set to PEC and its diagonal dimension is 450 mm. The battery has the following size 135 mm  $\times$  42 mm  $\times$  31 mm and is located inside the frame. The propellers are assumed to be flat in order to simplify the model.

Fig. 9 presents the simulated RCS signatures of different drone parts (i.e. one motor with propeller, drone frame only, and the battery) as well as, the full model. It can be observed that the impact of the drone frame is the largest so that the RCS of the full drone model is very close to that of the frame only. This is true for a fully PEC drone model, therefore, applicable to the carbon fiber drones. If the drone has dielectric arms, the effect of different parts may be more visible. Unfortunately, performing such simulations is not possible using IE in a reasonable time. This issue may be studied more carefully in the future. The battery effect on the total RCS is minor due to the location of the battery, which is visible only at  $\theta = 90^{\circ}$ ,  $\phi = 45^{\circ}$ . Undoubtedly, if the battery is located under the frame, it will have larger impact on the RCS since it will be visible from more observation angles assuming that the radar is located below the drone. The motor and the propeller have some effect, but it must be added that the





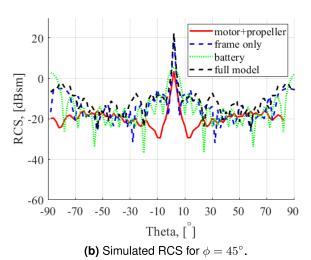


FIGURE 9. Simulated RCS signatures of different drone parts and full drone model.

propeller was approximated as a flat structure for simulation purposes, which might artificially increase its impact on the RCS. Under a plane wave illumination, a realistic curved propeller might distribute the reflected energy into a larger angular range thus resulting into smaller RCS.

Generally, it is possible to combine separate RCS of different objects to estimate the overall scattering pattern [20]. In practice, however, interactions between different elements might hamper such estimation. A drone may contain many wires and PCB boards which cannot be taken into account in universal simulations. Provided simulations present an estimation of the impact of different parts on the total RCS, while empirically obtained results give substantial drone characteristics.

### C. PRELIMINARY STATISTICAL DATA ANALYSIS

In this subsection, we present an insight on the statistical models of the RCS signatures and fit our measured data to one of these models. For complex and electrically large targets, the RCS varies several orders of magnitude as the observation angle changes. Thus, the RCS can be expressed synthetically using the simplified models. A common approach considers

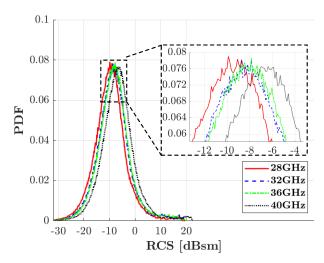


FIGURE 10. PDF of M100 at 28 GHz, 32 GHz, 36 GHz, and 40 GHz.

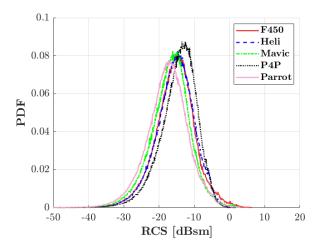


FIGURE 11. PDF of the measured RCS at 28 GHz for drone models from the Group I.

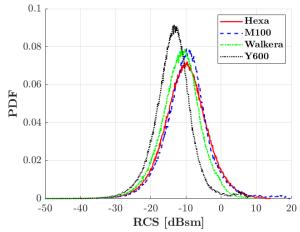


FIGURE 12. PDF of the measured RCS at 28 GHz for drone models from the Group II.

the RCS signature as a random variable represented by its associated probability density function (PDF). The complex variations of the RCS are then usually modelled by common statistical distributions (normal, log-normal, gamma,  $\chi^2$ , etc.) [21]–[23]. The statistical models are required by the



radar systems in order to decide if the observed radar bin contains a specific type of a target [24].

Fig. 10 shows the PDF for the DJI Matrice M100 across the measured frequency range. It can be seen that the distribution is shifted to higher RCS values with the increasing frequency. The probability density functions (PDFs) of the RCS for the two groups of drones are presented at 28 GHz in Figs. 11 and 12. Each data point of the PDF corresponds to the RCS value at a certain monostatic angle. Although the PDFs look approximately Gaussian, this assumption could not be verified through statistical tests. Hence, we restrict our analysis to the mean and standard deviation values. It can be noticed from Fig. 11 and Fig. 12 that the mean values of the second group are higher than those for the drones from the first group. Moreover, the highest RCS values are obtained for the drones made of carbon fiber materials.

## IV. CONCLUSIONS AND DISCUSSION

In this work, we presented the results of an extensive measurement campaign of the RCS signatures of diverse drone models at 26-40 GHz. Because drones are utilized in many different areas, it is crucial to detect malignant drones that are violating regulations and posing a threat to the public. Therefore, it is worthwhile to explore the use of mmWave frequencies for drone detection. The measurements show that larger drones made of carbon fiber material are easier to detect using radar systems. Moreover, the batteries installed on the drones contribute to the RCS significantly and might be detected even if the drone is small and made of non-reflective materials. For carbon fiber drones, the battery may have a small impact if it is installed inside the drone frame.

The main observations and measured values are summarized in the Appendix. It includes values of  $\mu$  (mean) and  $\sigma$  (standard deviation) of each distribution associated with each drone and for frequencies  $f \in \{26:2:40\}$  GHz as well as the maximum RCS values. Based on this measurement data, the following conclusions may be outlined.

- Mean RCS values of Group II are roughly 7 dB higher than those of Group I. This is predictable, since drones from Group II are mostly made of carbon fiber reinforced polymer material (CFRP) [19]. The dimensions of the drone also play an important role, as outlined in [9], [17], where similar variations in the RCS have been observed. It should be noted that this observation is not valid for the Y600. This model is the only one from Group II which was measured without the battery, hence smaller RCS values are obtained.
- Mean RCS increases with respect to the operating frequency, as observed in Fig. 10, and in [17], [19]. The rate at which the RCS increases does not depend on the drone model and is approximately equal to 0.25 dB/GHz.
- The standard deviation of the RCS is not impacted by the drone model and the operating frequency. For all the considered scenarios, σ is approximately 6 dB.
- For models that have been measured for both polarizations (Hexa, M100, Walkera, P4P and Y600)

the fitting parameters  $\mu$  and  $\sigma$  for the co-polar measurements (HH and VV) do not vary significantly. This observation is not valid for the cross-polarization measurements (only available for M100), where the mean and the maximal RCS are significantly lower than those of the co-polarization measurements. The cross-polarized component is low because the data samples are acquired in a quasi-monostatic configuration. Usually, this component increases when the transmitter and the receiver are not collocated [5].

• The maximum RCS of the drones from Group II is 10 to 20 dB higher than from the Group I. This is identified by the longer right tail of the PDFs of Hexa and M100 (Fig.12) and on the surface plots of the RCS (Fig.6). This large difference comes from the material of the drones. Drones from Group II are mainly made up of carbon while those from Group I are mostly made up of plastic. It has been demonstrated by simulations that the permittivity of the material significantly impacts the RCS [18]. Other parameters such as the geometry of the drone also have an impact on the RCS, but they are quite hard to describe due to the complexity of the scattering mechanisms.

The results presented in this work (available as a supplementary material<sup>3</sup>) can be used to form a substantial RCS database of commercially available drone models at different frequencies. This database would be a very valuable tool for future radar system operation. As future work, we are interested in extending this measurement campaign to perform measurements in other frequency bands as well as measuring a larger variety of drones.

The measured RCS signatures may provide useful information for future drone classification. Based on the measured RCS signatures, the drone model and/or pose might be identified (e.g. quadcopter, hexacopter) and safety measures can be undertaken if needed. Moreover, mmWave radars will be able to measure received signals from multiple angles at high spatial resolution over time. Future work can leverage these multi-measurement systems with machine learning algorithms for more complex identification tasks.

## APPENDIX SUMMARY OF THE OBTAINED RESULTS

See Table 2.

## **ACKNOWLEDGMENT**

The authors are particularly grateful to Viktor Nässi from the Department of Communications and Networking, Aalto University, assistant Professor Themistoklis Charalambous from the Department of Electrical Engineering and Automation, Aalto University, and Antti Lipasti from the "Vertical Hobby" for providing drone models for the measurements. The authors acknowledge the fruitful discussions in COST Action CA15104 IRACON. V. Semkin would like to acknowledge the support from Nokia Foundation, Jorma Ollila grant.



TABLE 2. Mean, standard deviation and maximal value of the RCS of each drone over the frequency range.

Mean, standard deviation and maximal value of the RCS of each drone over the frequency range

Model	26GF	28GHz		30GHz			32GHz			34GHz			36GHz			38GHz			40GHz				
	$\mu$ std	max	$\mu$	std	max	$\mu$	std	max	$\mu$	std	max	$\mu$	std	max	$\mu$	std	max	$\mu$	std	max	$\mu$	std	max
Group I																							
F450 (HH)	-17.1 5.9	3.3	-15.5	5.7	6.3	-16.1	6.2	7.6	-14.9	6.3	7.0	-15.7	6.3	8.0	-14.4	6.4	8.1	-14.2	6.1	8.3	-13.5	6.1	9.3
Helicopter (HH)	-17.3 5.8	6.3	-15.5	5.5	2.3	-16.3	5.7	8.6	-15.2	5.8	6.9	-15.6	5.9	5.4	-14.4	5.9	12.4	-14.0	5.8	8.8	-13.4	5.8	8.4
Mavic (HH)	-16.8 6.1	2.3	-16.8	5.6	2.4	-17.7	6.0	4.3	-16.7	6.3	6.5	-17.7	6.2	1.7	-16.0	6.3	7.1	-15.7	6.3	6.5	-15.0	6.2	7.5
Parrot (HH)	-19.5 6.2	4.6	-17.6	5.9	3.1	-18.0	6.0	5.7	-17.1	6.3	6.5	-17.8	6.3	8.2	-16.1	6.3	7.7	-15.7	6.3	9.5	-15.0	6.3	11.7
P4P (HH)	-16.4 5.6	2.6	-14.4	5.2	1.1	-14.2	5.4	3.0	-14.2	5.5	1.8	-15.6	5.5	2.5	-14.2	5.4	3.11	-13.2	5.5	2.5	-12.3	5.4	5.7
P4P (VV)	-15.7 5.5	0.1	-13.1	5.0	5.4	-14.6	5.5	3.8	-13.7	5.5	4.1	-15.1	5.5	2.6	-13.8	5.4	2.8	-12.9	5.4	4.6	-11.9	5.4	5.1
Group II																							
Hexa (HH)	-10.5 6.3	10.9	-10.1	6.3	14.0	-10.1	6.3	11.5	-8.8	6.4	12.6	-9.3	6.4	20.0	-7.9	6.4	14.0	-7.8	6.5	15.0	-7.2	6.5	16.6
Hexa (VV)	-10.5 6.2	11.4	-9.5	5.8	11.9	-9.3	6.2	12.2	-8.7	6.4	14.0	-10.0	6.4	12.8	-8.6	6.4	14.9	-7.9	6.4	15.8	-7.2	6.4	18.3
M100 (HH)	-10.5 6.8	15.8	-9.6	6.4	19.6	-8.6	6.4	16.0	-8.4	6.6	20.0	-9.7	6.6	20.5	-8.1	6.5	20.3	-7.4	6.5	19.7	-6.6	6.6	22.5
M100 (VV)	-10.0 6.5	14.8	-9.1	6.3	23.0	-8.5	6.4	17.8	-8.0	6.6	20.9	-9.1	6.5	18.3	-7.7	6.6	19.4	-7.0	6.5	20.0	-6.1	6.5	25.0
M100 (VH)	-17.2 5.4	0.1	-16.6	5.3	5.5	-13.9	5.5	5.0	-15.4	5.7	3.3	-15.5	5.9	4.0	-12.9	5.7	5.5	-13.2	5.6	5.8	-13.1	5.8	7.0
M100 (HV)	-17.8 5.5	-1.3	-18.3	5.8	1.2	-15.2	5.8	3.8	-16.1	5.9	3.5	-15.8	5.9	4.5	-12.6	5.6	6.1	-14.0	5.7	5.0	-13.6	5.7	7.2
Walkera (HH)	-12.6 6.1	8.1	-11.6	5.7	9.2	-10.5	5.8	9.4	-10.6	6.1	10.0	-12.2	6.1	8.4	-10.6	6.2	12.3	-9.7	6.0	11.0	-9.0	6.1	11.7
Walkera (VV)	-12.5 5.8	7.4	-11.4	6.7	9.9	-10.9	6.0	9.3	-10.3	6.1	11.5	-11.7	6.0	8.7	-10.1	6.0	12.6	-9.5	6.0	11.4	-8.5	5.9	13.2
Y600 (HH)	-16.8 6.5	6.3	-13.7	5.5	8.0	-13.6	5.9	8.1	-14.7	6.7	9.3	-16.2	6.7	9.7	-15.0	6.7	10.0	-13.8	6.5	13.5	-13.3	6.6	12.3
Y600 (VV)	-16.8 6.6	6.7	-13.6	5.5	8.8	-14.9	6.3	7.8	-14.8	6.8	11.8	-16.0	6.7	9.1	-15.0	6.8	11.8	-14.1	6.8	11.8	-13.0	6.6	12.3

#### **REFERENCES**

- L. Schroth. (Apr. 2019). The Drone Market 2019–2024: 5 Things to Know. [Online]. Available: https://www.droneii.com/the-drone-market-2019-2024-5-things-you-need-to-know
- [2] T. Schipper, J. Fortuny-Guasch, D. Tarchi, L. Reichardt, and T. Zwick, "RCS measurement results for automotive related objects at 23-27 GHz," in *Proc. 5th Eur. Conf. Antennas Propag. (EUCAP)*, Apr. 2011, pp. 683–686.
- [3] K. Geary, J. S. Colburn, A. Bekaryan, S. Zeng, B. Litkouhi, and M. Murad, "Automotive radar target characterization from 22 to 29 GHz and 76 to 81 GHz," in *Proc. IEEE Radar Conf. (RadarCon)*, Apr. 2013, pp. 1–6.
- [4] A. D. De Quevedo, F. I. Urzaiz, J. G. Menoyo, and A. A. Lopez, "Drone detection and RCS measurements with ubiquitous radar," in *Proc. Int. Conf. Radar (RADAR)*, Aug. 2018, pp. 1–6.
- [5] M. Röding, G. Sommerkorn, S. Häfner, R. Müller, R. S. Thomä, J. Goerlich, and K. Garhammer, "Fully polarimetric wideband RCS measurements for small drones," in *Proc. 11th Eur. Conf. Antennas Propag.* (EUCAP), Mar. 2017, pp. 3926–3930.
- [6] T. S. Rappaport, S. Sun, R. Mayzus, H. Zhao, Y. Azar, K. Wang, G. N. Wong, J. K. Schulz, M. Samimi, and F. Gutierrez, "Millimeter wave mobile communications for 5G cellular: It will work!" *IEEE Access*, vol. 1, pp. 335–349, 2013.
- [7] D. Solomitckii, M. Gapeyenko, V. Semkin, S. Andreev, and Y. Koucheryavy, "Technologies for efficient amateur drone detection in 5G millimeter-wave cellular infrastructure," *IEEE Commun. Mag.*, vol. 56, no. 1, pp. 43–50, Jan. 2018.
- [8] M. Caris, W. Johannes, S. Sieger, V. Port, and S. Stanko, "Detection of small UAS with W-band radar," in *Proc. 18th Int. Radar Symp. (IRS)*, Jun. 2017, pp. 1–6.
- [9] A. Herschfelt, C. R. Birtcher, R. M. Gutierrez, Y. Rong, H. Yu, C. A. Balanis, and D. W. Bliss, "Consumer-grade drone radar crosssection and micro-Doppler phenomenology," in *Proc. IEEE Radar Conf.* (*RadarConf*), May 2017, pp. 981–985.
- [10] J. Ochodnicky, Z. Matousek, M. Babjak, and J. Kurty, "Drone detection by Ku-band battlefield radar," in *Proc. Int. Conf. Mil. Technol. (ICMT)*, May 2017, pp. 613–616.

- [11] M. Guo, Y. Lin, Z. Sun, and Y. Fu, "Research on monostatic radar cross section simulation of small unmanned aerial vehicles," in *Proc. Int. Conf. Microw. Millim. Wave Technol. (ICMMT)*, May 2018, pp. 1–3.
- [12] M. Pieraccini, L. Miccinesi, and N. Rojhani, "RCS measurements and ISAR images of small UAVs," *IEEE Aerosp. Electron. Syst. Mag.*, vol. 32, no. 9, pp. 28–32, Sep. 2017.
- [13] M. I. Skolnik, Radar Handbook (Electronic Engineering Series). New York, NY, USA: McGraw-Hill, 1990.
- [14] D. G. Falconer, "Extrapolation of near-field RCS measurements to the far zone," *IEEE Trans. Antennas Propag.*, vol. AP-36, no. 6, pp. 822–829, Jun. 1988.
- [15] I. J. LaHaie, "Overview of an image-based technique for predicting far-field radar cross section from near-field measurements," *IEEE Antennas Propag. Mag.*, vol. 45, no. 6, pp. 159–169, Dec. 2003.
- [16] N.-J. Li, C.-F. Hu, L.-X. Zhang, and J.-D. Xu, "Overview of RCS extrapolation techniques to aircraft targets," *Prog. Electromagn. Res. B*, vol. 9, pp. 249–262, Jan. 2008.
- [17] C. J. Li and H. Ling, "An investigation on the radar signatures of small consumer drones," *IEEE Antennas Wireless Propag. Lett.*, vol. 16, pp. 649–652, 2017.
- [18] A. Schroder, M. Renker, U. Aulenbacher, A. Murk, U. Boniger, R. Oechslin, and P. Wellig, "Numerical and experimental radar cross section analysis of the quadrocopter DJI phantom 2," in *Proc. IEEE Radar Conf.*, Oct. 2015, pp. 463–468.
- [19] M. Ritchie, F. Fioranelli, H. Griffiths, and B. Torvik, "Micro-drone RCS analysis," in *Proc. IEEE Radar Conf.*, Oct. 2015, pp. 452–456.
- [20] M. I. Skolnik, Introduction to Radar Systems, 3rd ed. New York, NY, USA: McGraw-Hill, 2001.
- [21] W. Buller, B. Wilson, L. van Nieuwstadt, and J. Ebling, "Statistical modelling of measured automotive radar reflections," in *Proc. IEEE Int. Instrum. Meas. Technol. Conf. (IMTC)*, May 2013, pp. 349–352.
- [22] R. Guay, G. Drolet, and J. R. Bray, "Measurement and modelling of the dynamic radar cross-section of an unmanned aerial vehicle," *IET Radar, Sonar Navigat.*, vol. 11, no. 7, pp. 1155–1160, Jul. 2017.
- [23] X. Xu and P. Huang, "A new RCS statistical model of radar targets," *IEEE Trans. Aerosp. Electron. Syst.*, vol. 33, no. 2, pp. 710–714, Apr. 1997.



[24] M. A. Richards, Principles of Modern Radar. Raleigh, NC, USA: SciTech, 2010.



**VASILII SEMKIN** received the Lic. Sc. (Tech.) and D.Sc. (Tech.) degrees from the Aalto University School of Electrical Engineering, in 2014 and 2016, respectively. From 2016 to 2017, he was a Postdoctoral Researcher working on 5G antenna development with Aalto University, and then, from 2017 to 2018, with the Tampere University of Technology studying radio channel properties at mmWave frequencies. From 2018 to 2019, he was a Postdoctoral Researcher with the ICTEAM, Uni-

versité catholique de Louvain (UCLouvain, Louvain-la-Neuve, Belgium) working on wireless channel characterization, air-to-ground channel measurements, and drone detection. He is currently a Research Scientist with the VTT Technical Research Centre of Finland Ltd. His research interests include mmWave channel measurements and modeling, drone-aided communications, and reconfigurable antennas.



JAAKKO HAARLA was born in Helsinki, Finland, in 1987. He received the B.Sc. (Tech.) degree in electronics and the Diploma Engineering (M.Sc.) degree in radio science and engineering from Aalto University, Espoo, Finland, in 2015 and 2017, respectively. Since 2016, he has been with the Aalto University School of Electrical Engineering. His current research interests are the phased antenna arrays, antenna measurements, and IC integration at millimeter waves.



**THOMAS PAIRON** was born in Namur, in 1992. He received the B.Sc. and M.Sc. degrees in electrical engineering from UCLouvain, Louvain-la-Neuve, Belgium, in 2013 and 2015, respectively, where he is currently pursuing the Ph.D. degree with the Antenna Group and the Cosy Group. In 2016, he received a FRS FNRS-FRIA 4-years grant for pursuing his researches. His current researches encompass scattering by large curved structures, numerical simulations of large

antenna arrays, and propagation in indoor environment.



CHRISTOPHER SLEZAK (Student Member, IEEE) received the B.S. degree in electrical and computer engineering from Rutgers, The State University of New Jersey, in 2014. He is currently pursuing the Ph.D. degree with the NYU Tandon School of Engineering, Brooklyn, NY, USA. He is also a Researcher with the NYU WIRELESS. His research interests include wireless communications, millimeter wave channel measurements, and modeling of millimeter wave channel dynamics.



**SUNDEEP RANGAN** (Fellow, IEEE) received the Ph.D. degree from the University of California, Berkeley. He is currently a Professor of electrical and computer engineering with New York University and the Director of NYU WIRELESS. He co-founded (with four others) Flarion Technologies, which developed Flash-OFDM, the first cellular OFDM data system and precursor to 4G LTE. He was acquired by Qualcomm, where he was a director of engineering before joining NYU.



VILLE VIIKARI (Senior Member, IEEE) was born in Espoo, Finland, in 1979. He received the Master of Science (Tech.) and Doctor of Science (Tech.) (Hons.) degrees in electrical engineering from the Helsinki University of Technology (TKK), Espoo, Finland, in 2004 and 2007, respectively.

From 2001 to 2007, he was with the Radio Laboratory, TKK, where he studied antenna measurement techniques at submillimeter wavelengths and antenna pattern correction techniques. From

2007 to 2012, he was a Research Scientist and a Senior Scientist with the VTT Technical Research Centre, Espoo, where his research included wireless sensors, RFID, radar applications, MEMS, and microwave sensors. He is currently an Associate Professor and the Deputy Head of Department with the Aalto University School of Electrical Engineering, Espoo. His current research interests include antennas for mobile networks, RF-powered devices, and antenna measurement techniques.

Dr. Viikari was a recipient of the Young Researcher Award in 2014, presented by the Finnish Foundation for Technology Promotion, IEEE Sensors Council 2010 Early Career Gold Award, the 2008 Young Scientist Award of the URSI XXXI Finnish Convention on Radio Science, Espoo, and the Best Student Paper Award of the annual symposium of the Antenna Measurement Techniques Association, Newport, RI, USA, in 2005. He has served as the Chair of the Technical Program Committee of the ESA Workshop on Millimetre-Wave Technology and Applications and the Global Symposium on Millimeter Waves (GSMM) twice in Espoo, in 2011 and 2016.



**CLAUDE OESTGES** (Fellow, IEEE) received the M.Sc. and Ph.D. degrees in electrical engineering from the Université catholique de Louvain (UCLouvain), Louvain-la-Neuve, Belgium, in 1996 and 2000, respectively. In January 2001, he joined at the Smart Antennas Research Group (Information Systems Laboratory), Stanford University, Stanford, CA, USA, as a Postdoctoral Scholar. From January 2002 to September 2005, he was associated with the

Microwave Laboratory UCLouvain as a Postdoctoral Fellow of the Belgian Fonds de la Recherche Scientifique (FRS-FNRS). He is currently a Full Professor with the Electrical Engineering Department, Institute for Information and Communication Technologies, Electronics and Applied Mathematics (ICTEAM), UCLouvain. He is the author or coauthor of three books and more than 200 journal articles and conference communications. He has been the Chair of COST Action CA15104 (IRACON), since 2016. He was a recipient of the 1999–2000 IET Marconi Premium Award and the IEEE Vehicular Technology Society Neal Shepherd Award, in 2004 and 2012.

0 0 0